Journal of Ovonic Research Vol. 21, No. 6, November – December 2025, p. 845- 858

Fabrication of barium oxide nanoparticles as a promising thermal barrier coating for protecting corrosion in various metal surfaces

D. Vasudevan [a], K. Gowtham [a], S. Cheran [a], M. Venkatesan [b,*], P. Dineshkumar [c], A. Karthikeyan[d]
[a] *Department of Mechanical Engineering, K.S. Rangasamy College of Technology, Tiruchengode -637215, Tamil Nadu, India.*
[b] *Department of Mechanical Engineering, Excel Engineering College, Komarapalayam, Nammakal -637303, Tamil Nadu, India..*
[c]*Department of Agricultural Engineering, Kongunadu College of Engineering and Technology, Thottiam, Trichy -621215, Tamil Nadu, India.*
[d]*Department of Aeronautical Engineering, Excel Engineering College, Komarapalayam, Nammakal -637303, Tamil Nadu, India.*

Corrosion-induced material degradation is a critical global issue, causing annual economic losses and compromising the safety, performance, and service life of metallic infrastructure. Conventional protective coatings often degrade under aggressive service conditions, highlighting the need for multifunctional, environmentally benign corrosion inhibitors. In this study, barium titanate ($BaTiO_3$), a ferroelectric perovskite oxide with high dielectric constant, chemical stability, and strong barrier-forming capability, was synthesised via a hydrothermal route to yield phase-pure, highly crystalline nanoparticles with an average crystalline and particle size of 27.81 nm and d_{50} = 47.93 nm. $BaTiO_3$ coatings, applied via doctor-blade technique, were tested on copper, zinc, and mild steel (MS) substrates employing electrochemical impedance spectroscopy (EIS) and Tafel polarisation in 3.5% NaCl and acidic/alkaline media. In NaCl solution, inhibition efficiencies reached 88.74% (Cu), 86.92% (Zn), and 76.25% (MS), with positive Ecorr shifts and significant icorr reductions. In 1 M KOH, the efficiency for MS was 77.7%, while in 1 M HCl it was 48.82%, indicating better stability in alkaline media. To address reduced protection in acidic conditions, coating optimisation was performed by varying $BaTiO_3$ nanoparticle loadings (25, 50, 75, 100 mg). The 50 mg loading achieved the best performance in 2 M HCl, with Rp = 572.48 $\Omega \cdot cm^2$, η = 85.14%, and compact, defect-minimised surface coverage. Higher loadings led to coating heterogeneity, microcracks, and reduced inhibition, while lower loadings gave incomplete coverage. The optimisation strategy identified the nanoparticle concentration that maximises barrier integrity, dielectric shielding, and adhesion, establishing $BaTiO_3$ as a promising eco-friendly corrosion inhibitor for chloride-rich and industrial environments.

(Received September 28, 2025; Accepted December 19, 2025)

Keywords: Barium titanate, Perovskite, Corrosion inhibition, Hydrothermal

1. Introduction

Corrosion is a pervasive and inevitable phenomenon that affects metals and alloys through electrochemical or chemical reactions with their surrounding environment. It leads to the progressive degradation of materials, resulting in reduced structural integrity, compromised safety, and increased maintenance demands. As a global industrial challenge, corrosion impacts nearly every sector, including oil and gas, transportation, marine, power generation, infrastructure, and manufacturing, making it a critical concern for engineers, policymakers, and economists alike [1,2]. The worldwide economic losses attributed to corrosion are staggering [3]. This encompasses direct costs, such as repair, replacement, and preventive maintenance, as well as indirect costs, including construction downtime, loss of efficiency, and environmental damage. In addition to financial burdens, corrosion-related failures can cause catastrophic accidents, endanger human life, and lead to environmental pollution through leakage of hazardous substances.

Corrosion prevention strategies encompass a range of material, chemical, and electrochemical approaches aimed at mitigating or delaying metal degradation. Protective coatings, including polymeric paints, metallic platings (such as zinc, nickel, or chromium), and advanced ceramic layers, serve as physical barriers that isolate

* Corresponding author: venkatesanm1972@gmail.com
https://doi.org/10.15251/JOR.2025.216.845

the substrate from corrosive agents [4–6]. Organic or inorganic corrosion inhibitors are introduced into the environment to suppress anodic or cathodic processes by creating protective passive films over the metal surface [7–9]. Cathodic protection, implemented either through sacrificial anodes (galvanic protection) or impressed current systems, shifts the metal potential to a level where corrosion is thermodynamically unfavourable. Material selection and alloy design also play a vital role, with corrosion-resistant alloys such as stainless steels, (IV) and aluminium alloys offering inherent protection [10–12]. Environmental control, such as dehumidification, pH regulation, and removal of aggressive ions like chlorides, further reduces corrosion risks. Increasingly, nanomaterial-based coatings and self-healing systems are emerging as advanced solutions, offering enhanced barrier properties, tailored surface chemistry, and long-term durability [13,14].

Barium titanate ($BaTiO_3$), a ferroelectric perovskite oxide, has emerged as a promising functional additive in corrosion protection coatings owing to its unique structural, electrical, and chemical properties [15,16]. Its high dielectric constant and ferroelectric polarisation enable it to store and redistribute charges at the coating-metal interface, thereby suppressing localised electrochemical reactions that initiate corrosion. The chemically stable perovskite structure of $BaTiO_3$ offers excellent resistance to acidic and alkaline environments, while its wide band gap (~3.2 eV) imparts strong insulating behaviour, reducing electron transfer between the metal substrate and corrosive species. Furthermore, $BaTiO_3$ nanoparticles exhibit high surface activity, enabling dense packing within polymer matrices and effectively blocking pathways for water, oxygen, and chloride ion ingress [17–19]. Its inherent non-toxicity and environmental compatibility make it a sustainable alternative to conventional toxic inhibitors. Moreover, the piezoelectric and ferroelectric properties of $BaTiO_3$ promote passive film formation when subjected to mechanical or electrochemical stimuli, thereby improving the coating's self-healing capability. These synergistic properties make $BaTiO_3$ a highly effective corrosion inhibitor, capable of significantly enhancing the barrier performance, adhesion strength, and long-term durability of protective coatings on metallic substrates.

Thus, this study employs a hydrothermal technique to tune the morphology of annaoparticles effectively. The hydrothermal technique is particularly advantageous for synthesising $BaTiO_3$ perovskite nanoparticles due to its ability to produce high-purity, well-crystallised materials at relatively low temperatures and pressures. This method facilitates controlled crystal growth directly from aqueous solutions, allowing for the precise tuning of particle size, morphology, and phase composition without requiring high-temperature calcination, which often induces grain coarsening. The closed-system environment minimises contamination and allows the use of mild reaction conditions, reducing energy consumption. Additionally, the hydrothermal process promotes uniform nucleation, leading to nanoscale $BaTiO_3$ with high surface area and enhanced functional properties critical for improving dispersion, barrier performance, and electrochemical stability in corrosion protection coatings.

2. Experimental procedure

2.1 Materials required

Barium nitrate (≥99%) ($Ba(NO_3)_2$), Ammonium Hydroxide (NH_4OH), (IV) isopropoxide ($Ti(OCH(CH_3)_2)_4$), Double-Distilled (DD) water, and Ethanol (99%). The synthesis process involved ethanol and DD water in the production of $BaTiO_3$ NPs. All reagents used in this work were of analytical grade and procured from Sigma Aldrich, India. For electrochemical studies, zinc, Copper, and mild steel (MS) plates were purchased with a thickness of 1 mm. Additionally, N-methyl-2-pyrrolidone (NMP) was used as a solvent for coating in corrosion analysis, and Polyvinylidene fluoride (PVDF) was used as a binder.

2.2 Synthesis of $BaTiO_3$ NPs through the hydrothermal technique

For the synthesis, 0.01 mol of $Ba(NO_3)_2$ was dissolved in 40 mL of a 1:1 (v/v) ethanol-water mixture, stirred under magnetic conditions to yield a clear solution. Separately, 0.01 mol of (IV) isopropoxide was diluted in 20 mL of ethanol and introduced dropwise into the barium nitrate solution with continuous stirring. The reaction pH was adjusted to 10.5 using NH_4OH, followed by stirring for 1 h to achieve a uniform precursor suspension. This mixture was transferred into a Teflon-lined stainless-steel autoclave, sealed, and subjected to hydrothermal treatment at 180 °C for 12 h. After cooling naturally to ambient temperature, the resulting precipitate was collected by centrifugation, thoroughly washed with DD water and ethanol to eliminate residual impurities, and dried at 80 °C for 12 h. Finally, the dried powder was calcined at 650 °C for 2 h to obtain phase-pure $BaTiO_3$ nanoparticles. A schematic representation of the synthesis route is provided in Fig. 1.

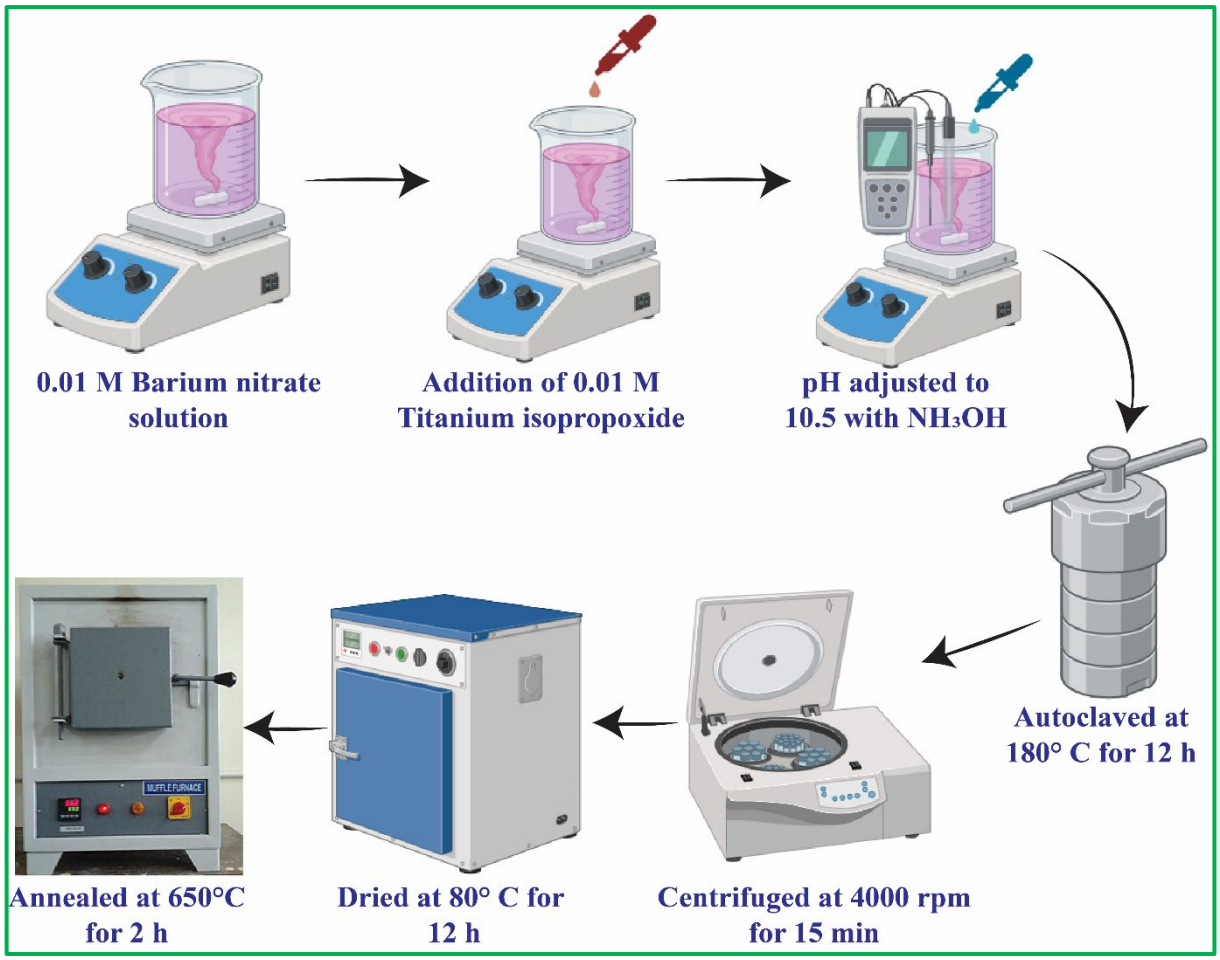

Fig. 1. Schematic representation of methodology for the synthesis of $BaTiO_3$ NPs.

2.3 Characterisation techniques

The crystallographic properties of the prepared BaTiO3 NPs were analysed using X-ray Diffraction (XRD) (X' Pert Pro-PAnalytic). Similarly, functional group analysis was carried out using Fourier transform infrared spectroscopy (FTIR) (Shimadzu, Japan; Thermo Fisher Scientific, USA; IRAffinity-1, Thermo Nicolet iS50 with an inbuilt ATR). Furthermore, the morphology and particle size of the prepared $BaTiO_3$ NPs were analysed using a Field emission scanning electron microscope (FESEM) (Quanta FEG 250) and particle size analyser (PSA) (Anton Paar, Litesizer 500)

2.4 Electrochemical studies

Corrosion behaviour was evaluated in a three-electrode cell using a Metrohm AUTOLAB PGSTAT (FRA module; NOVA). The working electrode (WE) (10 × 10 × 2 mm) was coated with a $BaTiO_3$ slurry at a mass ratio of 80:15:5 ($BaTiO_3$: NMP: PVDF, wt%). For the slurry, PVDF (5 wt%) was first dissolved in NMP (15 wt%) at 60 °C under stirring (30–45 min) to form a clear binder solution; $BaTiO_3$ powder (80 wt%) was then added and dispersed by ultrasonication (15 min) followed by high-shear stirring (30 min) to obtain a homogeneous, bubble-free ink. Pre-polished working electrode, ultrasonically cleaned in ethanol and DD water, was coated by the doctor-blade technique. Coatings were flashed at 60 °C for 30 min to evaporate excess NMP. The exposed area was defined as 1 cm^2. An Ag/AgCl (3 M KCl) reference electrode (Luggin tip 2–3 mm from WE) and a Pt-mesh counter electrode (≥2 cm^2) completed the cell. Tests were conducted in a naturally aerated electrolyte at 25 ± 1 °C after 30 minutes with a potential window of –2 to 0 V.

3. Results and discussion

3.1 Crystallographic analysis

Fig. 2 (a) represents the XRD spectrum of the prepared BaTiO3 NPs, where the highly crystalline peaks were observed. The characteristic peaks were observed at the 2θ positions 22.27 °, 31.72°, 39.02°, 45.27°, 56.22°, 66.12°, and 74.92°, which are indexed to (101), (012), (021), (202), (122), (220), and (214) Miller indices. The obtained indexed peaks can be matched with the hexagonal crystal structure phase of $BaTiO_3$ perovskite, which belongs to the R3m space group, as indexed in the JCPDS card number 96-901-4075 [20,21]. The crystalline size of the prepared BaTiO3 NPs is calculated using the Debye-Scherrer equation [22].

$$D = \frac{K\ \lambda}{\beta\ cos\theta}$$

The calculated average crystalline size of the prepared BaTiO3 NPs is 27.81 nm as provided in Table 1. To further investigate the changes in crystalline size caused by intrinsic stress and strain, the W-H method was used to calculate the crystalline size, as shown in Fig. 2(b). The crystalline size calculated using the WH plot method was 38.21, a minor discrepancy with the Debye and the WH plot can be accounted for by the calculation involving stress and strain present in the material. Overall, the XRD results confirm phase-pure, highly crystalline $BaTiO_3$ with nanoscale domains and a small but measurable microstrain (~3.6×10^{-3}), consistent with the chosen hydrothermal route producing well-crystallised particles at relatively low temperature.

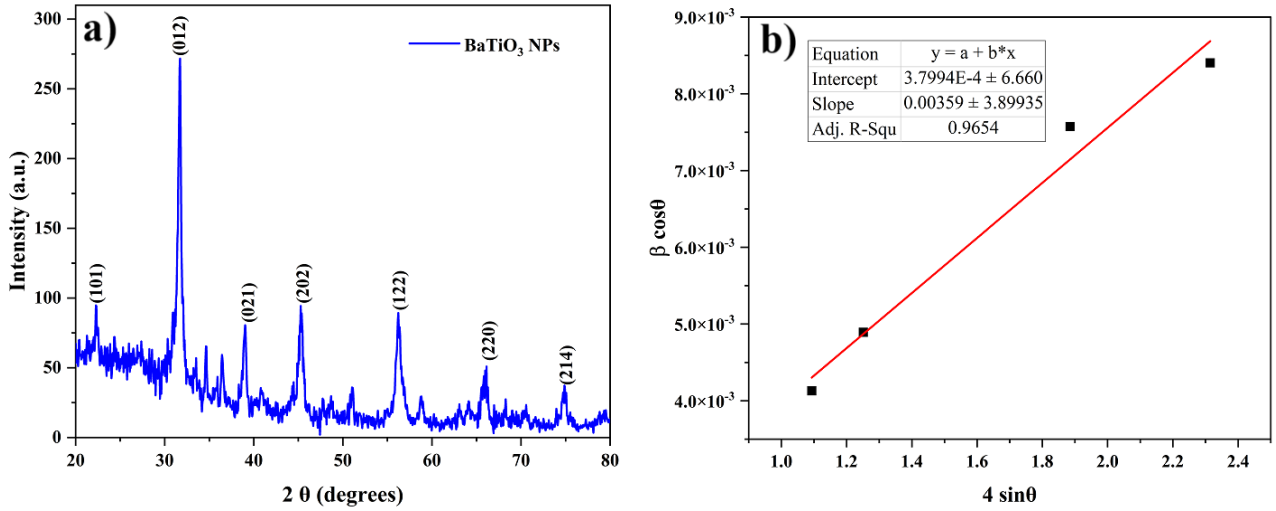

Fig. 2. Crystallographic analysis of $BaTiO_3$ NPs (a) XRD spectrum and (b) W-H plot.

Table 1. Crystallographic properties of prepared $BaTiO_3$ NPs.

Space group	R 3 m
Crystalline Size (Debye Scherrer)	27.81 nm
Crystalline size (W-H)	38.21 nm
Dislocation density	1.29 x 10^{-3} lines/m^2
Micro strain	3.59 x 10^{-3} ε

3.2 Functional group analysis

Fig. 3 presents the FTIR spectrum of the hydrothermally synthesised $BaTiO_3$ nanoparticles in the range of 4000–400 cm^{-1}. A broad absorption band centred at 3418 cm^{-1} is attributed to the O-H stretching vibrations of adsorbed water molecules and surface hydroxyl groups, commonly present due to ambient moisture adsorption on oxide nanoparticle surfaces [23]. The peak observed at 1627 cm^{-1} corresponds to the bending vibration (δ-H-O-H) of molecular water, further confirming the presence of physisorbed water [24]. A weak band at 1408 cm^{-1}

can be attributed to carbonate species (C-O) resulting from atmospheric CO_2 adsorption or residual barium carbonate traces formed during synthesis [25].

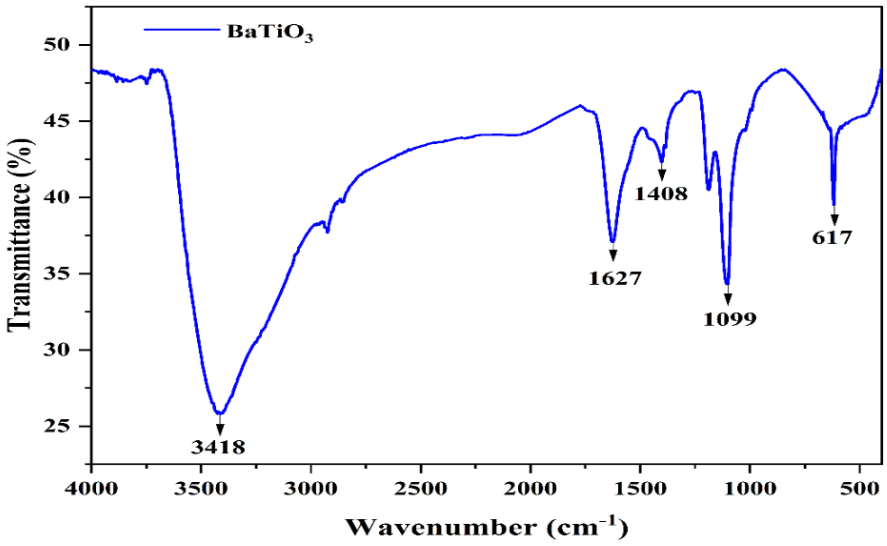

Fig. 3. FTIR spectra of the prepared $BaTiO_3$ NPs.

The absorption at 1099 cm^{-1} is generally assigned to Ti-O bond stretching within the TiO_6 octahedra, indicative of the short-range structural order in the perovskite lattice [26]. The strong low-wavenumber band at 617 cm^{-1} is characteristic of Ba-O-Ti stretching vibrations, confirming the formation of the $BaTiO_3$ perovskite phase [27]. This fundamental vibration is associated with the asymmetric stretching of Ti-O bonds in the TiO_6 octahedra, a structural motif central to the ferroelectric and dielectric properties of $BaTiO_3$. The absence of intense peaks in the 800–900 cm^{-1} region, where Ti-O-Ti vibrations from anatase TiO_2 typically appear, supports the phase purity inferred from XRD results [28]. Overall, the FTIR analysis corroborates the XRD findings, confirming the formation of phase-pure $BaTiO_3$ nanoparticles with characteristic Ba-O-Ti bonding, while also indicating the presence of minor surface-adsorbed water and carbonate species, which is typical for hydrothermally prepared oxide powders exposed to ambient conditions.

3.3 Morphology analysis

Fig. 4(a–b) presents the field emission scanning electron microscopy (FESEM) micrographs of the hydrothermally synthesised $BaTiO_3$ NPs at different magnifications. At lower magnification (200 nm), the particles exhibit a densely packed arrangement, indicating the formation of an interconnected granular network. The morphology appears to be composed of near-spherical to slightly faceted particles, aggregated into secondary clusters. This agglomeration is expected for oxide nanoparticles due to their high surface energy and the existance of interparticle van der Waals forces. At higher magnification Fig. 4(b), individual nanoparticles can be resolved more clearly, revealing a predominantly polyhedral morphology with well-defined crystallographic facets, consistent with the perovskite structure of $BaTiO_3$ [29]. The particle sizes observed range between ~40–80 nm, which is in reasonable agreement with the hydrodynamic size obtained from DLS (~47.93 nm) and slightly larger than the XRD-derived crystallite size (~28–38 nm), the difference being attributable to the presence of polycrystalline aggregates and possible surface-adsorbed species. The sharp-edged grain morphology suggests that the hydrothermal synthesis conditions, such as controlled temperature and precursor concentration, promoted a highly crystalline growth process with minimal amorphous phase formation [30]. The uniform grain size distribution observed is advantageous for maintaining consistent dielectric properties, as $BaTiO_3$ exhibits size-dependent ferroelectric behaviour near the nanoscale regime [31].

Furthermore, the compact packing visible in the micrographs is beneficial for applications where high density and minimal porosity are desired, such as in capacitor dielectrics or protective coatings. No significant presence of elongated rod-like structures or irregular platelets was observed, indicating that the chosen synthesis

parameters favoured isotropic crystal growth rather than anisotropic morphologies. The absence of large voids or macropores also suggests a high degree of homogeneity, which is consistent with the phase-pure nature confirmed by XRD and the characteristic Ba-O-Ti vibrations observed in FTIR analysis.

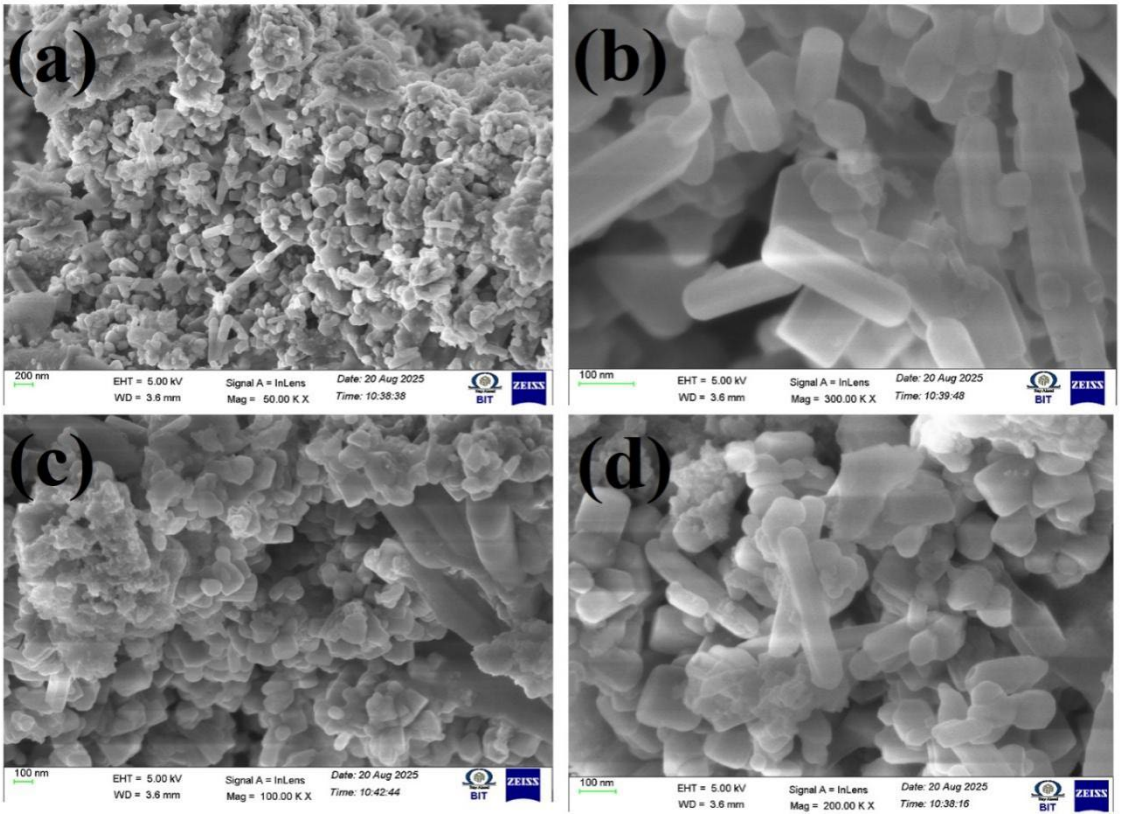

Fig. 4. FESEM morphology of the prepared $BaTiO_3$ NPs.

3.4 Particle size analysis

Fig. 5 illustrates the particle size distribution of the hydrothermally synthesised $BaTiO_3$ nanoparticles as determined by dynamic light scattering (DLS). The distribution exhibits a unimodal pattern, indicating a relatively uniform particle size population without significant secondary agglomeration peaks. The calculated median particle size (d_{50}) is approximately 47.93 nm, which lies within the expected range for nanoparticles synthesised via controlled hydrothermal processing. The relatively narrow distribution profile observed in Fig. 5 suggests that the synthesis parameters, particularly precursor concentration, pH control, and temperature profile, were effective in suppressing excessive grain growth and polydispersity. The absence of large-size peaks beyond 200 nm indicates minimal formation of hard agglomerates, which is advantageous for applications requiring high surface area and homogeneous dispersion, such as dielectric ceramic fabrication, polymer composite reinforcement, and functional coating formulations. Moreover, the d_{50} value obtained here aligns well with previous reports for hydrothermally prepared $BaTiO_3$ nanoparticles, confirming that the adopted synthesis route yields nanoscale particles with controlled size distribution. This controlled particle size is critical for tailoring the ferroelectric, dielectric, and piezoelectric properties of $BaTiO_3$, as these are known to be size-dependent near the nanoscale regime.

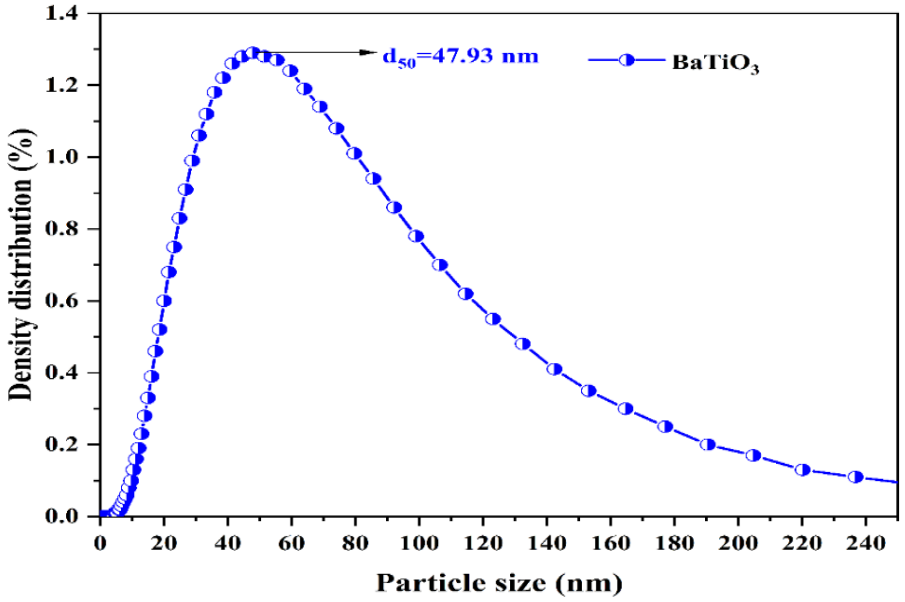

Fig. 5. Particle size analysis of prepared $BaTiO_3$ NPs.

3.5 Electrochemical analysis

3.5.1 Corrosion analysis on different substrates

The electrochemical impedance analysis (Nyquist plot) of different substrates, including copper, Zinc, and MS plates with both uncoated and coated $BaTiO_3$ nanoparticles in 3.5% NaCl, is represented in Fig. 6. The obtained Nyquist plot for the bare plate (Cu, Zn, and MS) shows a small semicircle in the lower frequency region, suggesting that the plates are more prone to corrosion with lower charge transfer resistance. This can be attributed to the absence of a protection film on the Cu, Zn, and MS plates, and the presence of chloride ions in the NaCl electrolyte, which rapidly interact with the metal surfaces, promoting dissolution and driving electrochemical reactions that result in corrosion [32]. In contrast, the $BaTiO_3$-coated plates exhibit a marked alteration in impedance behaviour, characterized by an enlarged arc in the spectra, indicating an increase in charge transfer resistance. Notably, the charge transfer resistance of Cu, Zn, and MS increased to 506.48 Ω/cm^2, 414.73 Ω/cm^2, and 198.39 Ω/cm^2, respectively, with the protective $BaTiO_3$ coating. The increase in impedance values clearly reflects the effectiveness of this barrier in preventing localised corrosion attack and minimising the electrochemical activity of copper in the saline solution [33]. This is possibly due to the protective layer of $BaTiO_3$ NPs, which effectively prevents the diffusion of chloride ions to interact with the metal surface, perhaps helping to prevent corrosion.

The Tafel polarisation curves for uncoated and $BaTiO_3$-coated Cu, Zn, and MS substrates, presented in Fig. 7, reveal pronounced alterations in the electrochemical response within a 3.5% NaCl solution. For the uncoated metals, the measured corrosion potentials (E_{corr}) were –0.468 V for Cu, –1.389 V for Zn, and –0.997 V for MS, as summarised in Table 2. Correspondingly, the bare substrates exhibited elevated corrosion current densities (i_{corr}), signifying an accelerated corrosion rate due to the unhindered ingress of chloride ions (Cl^-) and associated depassivation of the metal surface. This behaviour underscores the vulnerability of unprotected metals to chloride-induced electrochemical attack [34]. Upon application of the $BaTiO_3$ coating, a distinct shift in E_{corr} toward more noble potentials was observed, accompanied by a substantial reduction in i_{corr} for all substrates. These changes indicate a marked suppression of both anodic dissolution and cathodic oxygen reduction kinetics, demonstrating the coating's capacity to impede charge transfer processes at the metal-electrolyte interface. The calculated corrosion inhibition efficiencies were 88.74% for Cu, 86.92% for Zn, and 76.25% for MS, confirming that $BaTiO_3$ provides robust protection across multiple metallic systems.

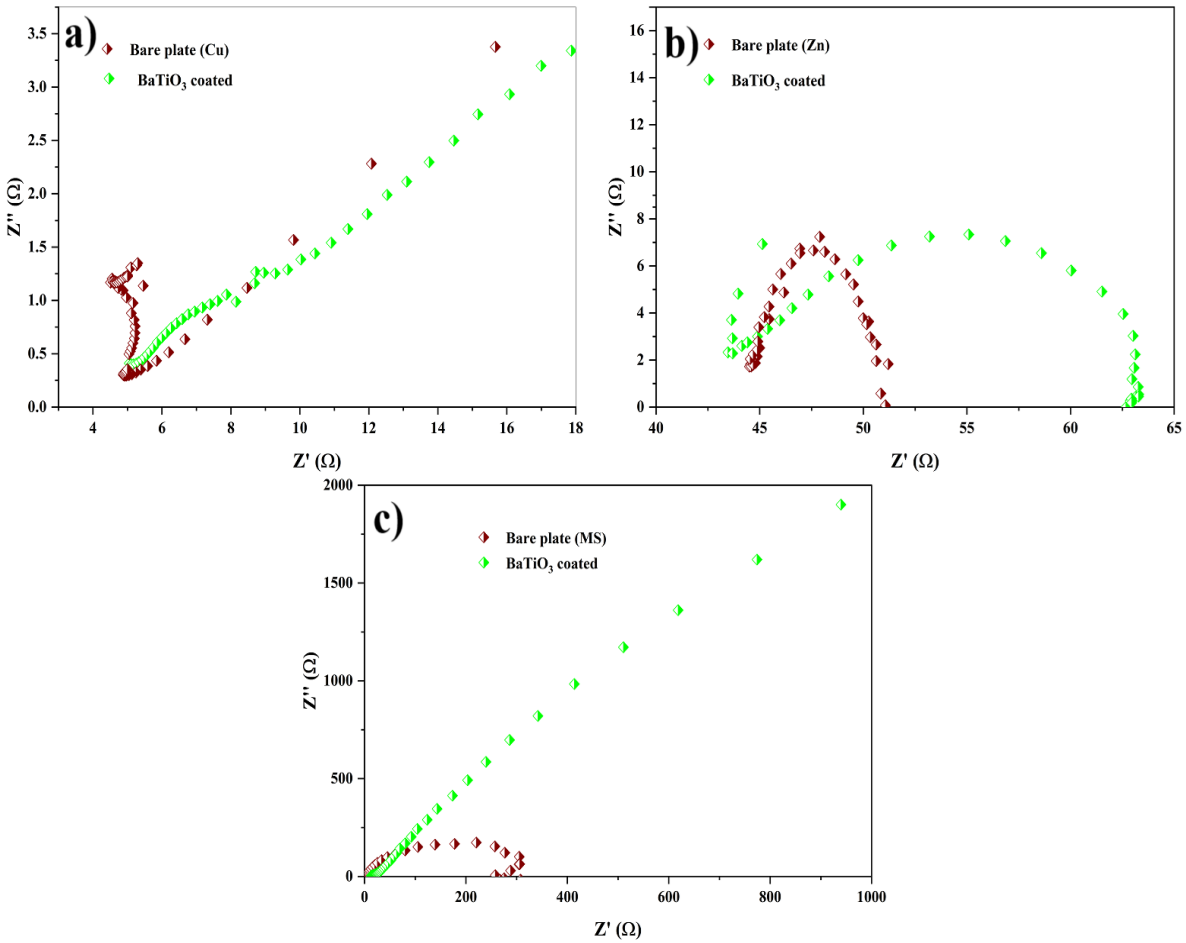

Fig. 6. Nyquist plot for different coated and uncoated metal surfaces, such as (a) Cu plate, (b) Zn plate, and (c) MS plate.

The protective action of $BaTiO_3$ is attributed to its ability to form a dense, adherent ceramic layer that serves as an effective physical barrier against Cl^- ingress, oxygen, and water. The perovskite-type oxide lattice of $BaTiO_3$ is chemically stable, with intrinsically low ionic and electronic conductivities, thereby restricting the transport of corrosive species. Furthermore, its high hardness and low porosity minimize the occurrence of microstructural defects, such as pinholes or cracks, that can serve as initiation sites for localized corrosion [35]. An additional factor may involve dielectric shielding effects arising from the high permittivity of $BaTiO_3$, which could alter double-layer capacitance and suppress interfacial electrochemical activity. Collectively, these attributes account for the observed reduction in corrosion current density and the shift toward more noble corrosion potentials, establishing $BaTiO_3$ as a promising multifunctional barrier coating for chloride-rich environments.

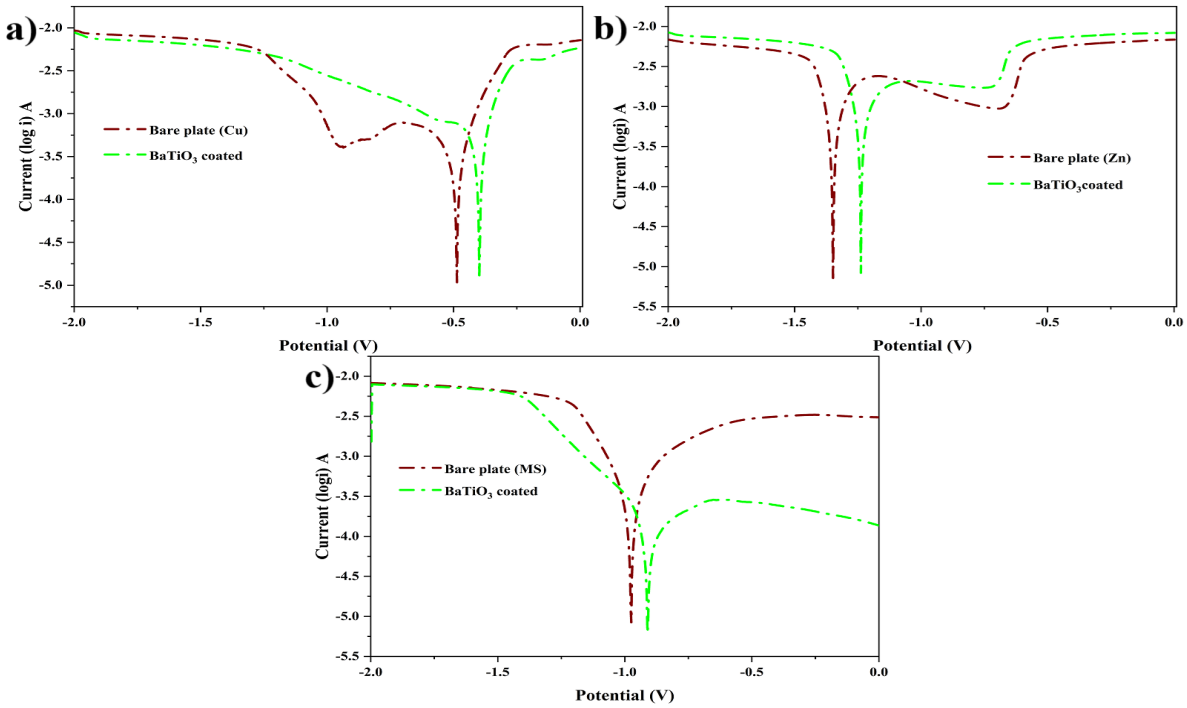

Fig. 7. Tafel polarisation plot for different metal surfaces (coated and uncoated), such as (a) Cu plate, (b) Zn plate, and c) MS plate.

From the comparative analysis of different metal surfaces, it is observed that the Zn plate is more prone to corrosion due to its more negative standard electrode potential ($E° \approx –0.76$ V vs SHE), making it more anodic and reactive. Furthermore, the more negative E_{corr} values obtained for the Zn plate also confirm the highly susceptible nature of the material to be corroded. However, the employed $BiTiO_3$ coating has significantly improved the corrosion resistance of the Zn plate. In the chosen substrate with the lower E_{corr}, the bare copper plate is more resistant and noble against corrosion. While examining the electrochemical behaviour of the MS plate, the E_{corr} rate is comparatively higher, and the $BaTiO_3$ coating has also provided lower corrosion resistance when compared to other metal substrates. While examining the usage of metal substrates, MS plates are widely employed in construction, infrastructure, the automotive industry, machinery, and pipelines. The extensive use of MS plates is primarily due to their lower cost compared to copper and zinc, making them a more economical choice for large-scale structural and industrial applications. Additionally, it offers high tensile strength and toughness suitable for construction, machinery, pipelines, and automotive frames. Thus, optimising corrosion protection for MS plates is crucial to extending the lifespan of MS plates used in various mechanical applications. Initially, it is essential to analyse the electrochemical behaviour of the MS plate in various electrolytes.

Table 2. Polarisation electrochemical parameters of different metal surfaces in 3.5 % NaCl medium.

Substrate	Coating	Ecorr (V)	Icorr (A)	Polarisation Resistance (Ω)	Corrosion rate (mm/year)	Efficiency (%)
Copper plate	Uncoated	–0.468	0.00075	59.685	8.59	-
	$BiTiO_3$ coated	–0.397	6.51×10^{-5}	174.2	0.967	88.74
Zinc Plate	Uncoated	–1.389	0.00598	23.747	46.97	-
	$BiTiO_3$ coated	–1.227	0.00051	33.116	6.14	86.92
MS plate	Uncoated	–0.997	0.00017	256.98	1.7238	-
	$BiTiO_3$ coated	–0.901	3.41×10^{-5}	803.45	0.4093	76.25

3.5.2 Electrochemical impact of acidic and alkaline media on MS substrates

The Nyquist plots, presented in Fig. 8 (a and c), clearly demonstrate the distinct electrochemical behaviours of the uncoated and coated specimens in 1M KOH and 1 M HCl electrolyte. For the bare MS plate, the impedance spectra display depressed semicircles in the low-frequency region, indicative of rapid charge transfer processes and insufficient barrier protection, which is characteristic of highly corrosive interaction between the electrolyte and the metal substrate. This behaviour is more pronounced in the acidic medium (HCl) due to aggressive proton attack and accelerated dissolution kinetics. In contrast, the $BaTiO_3$-coated MS plate exhibits a significant enlargement of the semicircle diameter in both electrolytes, reflecting an increase in charge transfer resistance to 544.74 Ω/cm^2 in 1 M KOH and 155.74 Ω/cm^2 in 1 M HCl. This enhancement confirms that the $BaTiO_3$ layer effectively retards electrochemical reactions by impeding the movement of corrosive species towards the metal surface. The broader impedance arc also suggests improved capacitive behaviour, likely due to the dielectric nature of $BaTiO_3$, which enhances double-layer stability and reduces interfacial reactivity.

Tafel polarisation curves, shown in Fig. 8(b) and (d), further corroborate the EIS findings. The coated MS plate exhibits a pronounced positive shift in corrosion potential in both electrolytes, accompanied by a significant decrease in corrosion current density. This behaviour reflects the inhibition of anodic metal dissolution as well as cathodic hydrogen or oxygen reduction processes [36]. The calculated corrosion inhibition efficiencies for $BaTiO_3$-coated MS were 77.7% in 1 M KOH and 48.82% in 1 M HCl, as summarised in Table 3. The higher inhibition efficiency in alkaline medium can be attributed to the relative chemical stability of $BaTiO_3$ under basic conditions, where it resists dissolution and maintains coating integrity [37]. In acidic media, partial leaching or structural degradation of $BaTiO_3$ may occur, leading to reduced protective performance. Given that the corrosion rate of the $BaTiO_3$-coated MS plate was significantly higher in 1 M HCl compared to 1 M KOH, further optimisation studies are underway to enhance protective performance in acidic environments.

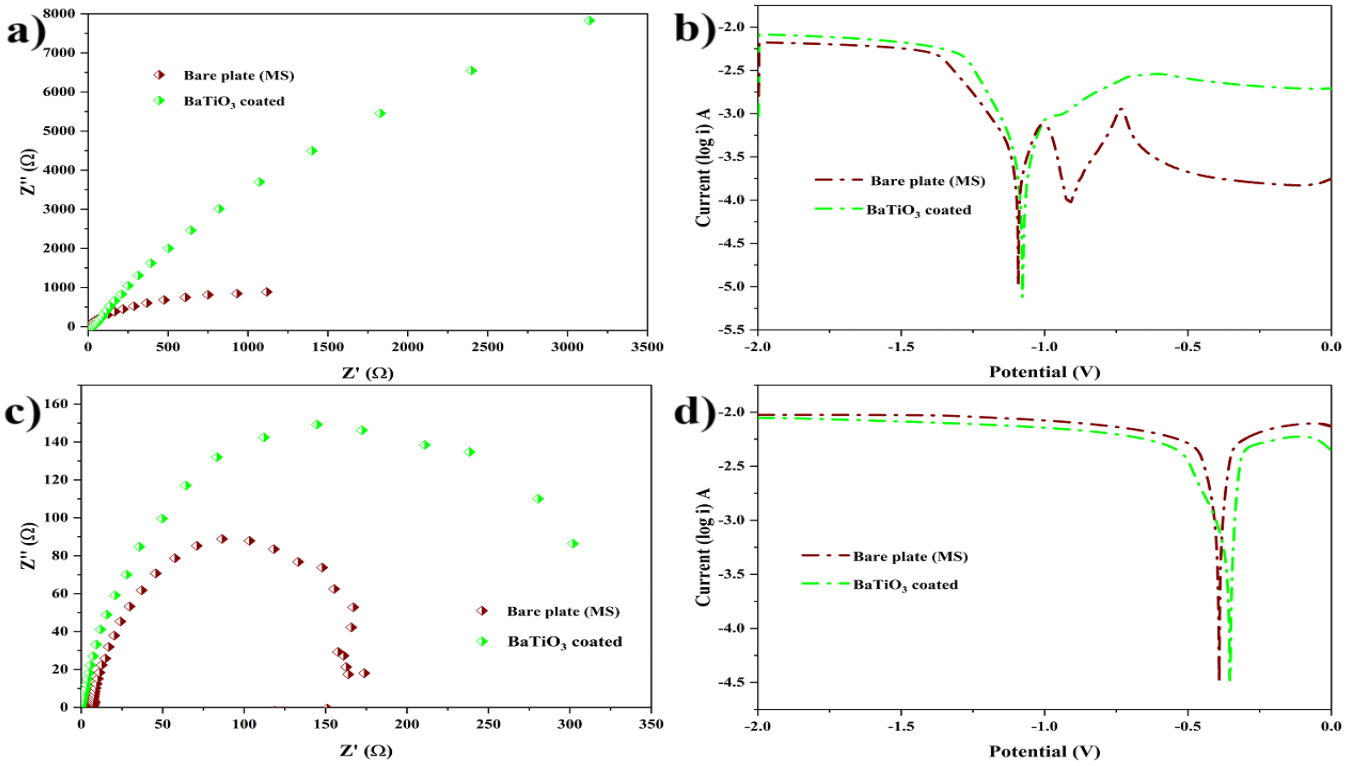

Fig. 8. Nyquist and Tafel plot of Bare and coated MS plate in KOH (a and b) and HCl (c and d).

Table 3. Polarisation electrochemical behaviour of coated and uncoated MS plates in basic and acidic electrolytes.

Electrolyte	Coating	Ecorr (V)	Icorr (A)	Polarisation Resistance (Ω)	Corrosion rate (mm/year)	Efficiency (%)
KOH	Uncoated	–1.092	0.00019	94.14	2.276	-
	$BiTiO_3$ coated	–1.0763	0.00017	337.91	0.506	77.7
HCl	Uncoated	–0.3915	0.00154	14.649	17.9	-
	$BiTiO_3$ coated	–0.3533	0.00078	19.69	9.16	48.82

3.5.3 Optimisation of $BaTiO_3$ Loading for Corrosion Resistance

In the initial formulation, a coating loading of 10 mg $BaTiO_3$ was employed; however, to improve barrier integrity and resistance to proton-assisted degradation, incremental increases in $BaTiO_3$ content are being investigated. The revised coating compositions incorporate $BaTiO_3$ at loadings of 25 mg, 50 mg, 75 mg, and 100 mg, enabling a systematic evaluation of how increased nanoparticle concentration influences coating density, defect minimisation, and overall corrosion inhibition efficiency in 2 M HCl electrolyte. This approach aims to identify an optimal loading that maximises coverage uniformity and stability in aggressive acidic media without compromising mechanical adhesion or introducing coating brittleness.

The Nyquist plots in Fig. 9(a) exhibit distinct differences in the diameter of the capacitive semicircles, directly correlating with the charge transfer resistance (R_p) values presented in Table 4. For the bare MS plate, a small semicircle was observed with an R_p of 115.64 Ω/cm^2, indicating rapid charge transfer and high corrosion activity due to the aggressive chloride and proton attacks in the acidic environment. Upon coating with 25 mg $BaTiO_3$, the semicircle diameter increased moderately, corresponding to an R_p of 178.31 Ω· cm^2, indicating an improvement in corrosion resistance due to partial surface coverage and barrier formation. The most significant enhancement was observed at a 50 mg loading, where the R_p value increased sharply to 572.48 Ω·cm^2, indicating optimal coating density and minimal defect pathways for ion transport. This suggests that 50 mg $BaTiO_3$ offers the best balance between coating continuity, thickness, and adhesion, effectively restricting Cl^- penetration and slowing down anodic dissolution.

However, further increases in $BaTiO_3$ loading to 75 mg and 100 mg resulted in a reduction of R_p values to 134.11 Ω/cm^2 and 52.084 Ω/cm^2, respectively. This decline can be attributed to excessive particle deposition, leading to coating heterogeneity, microcrack formation due to internal stress, and poor adhesion, which create preferential pathways for electrolyte ingress. The sheet resistance (R_s) values also support this trend, with the lowest R_s (1.2028 Ω/cm^2) observed for the 100 mg loading, indicating higher ionic conductivity at the interface due to coating defects.

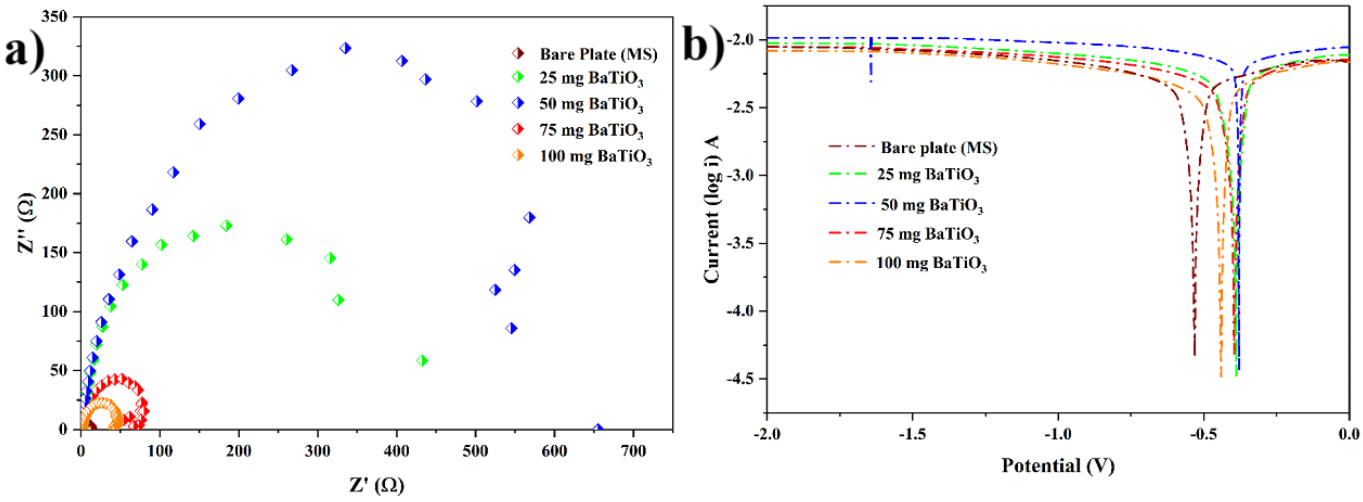

Fig. 9. Effect of $BaTiO_3$ loading on MS plate and their electrochemical characteristics (a) Nyquist plot and (b) Tafel plot.

Table 4. Impedance characteristics of the MS plate coated with various concentrations of $BaTiO_3$.

Medium	Substrate	Rp.R	Rs.R	CPE.N
2 M HCl	Bare	115.64	1.5033	0.99607
	25 mg $BaTiO_3$	178.31	20.279	0.9993
	50 mg $BaTiO_3$	572.48	1.8624	0.99858
	75 mg $BaTiO_3$	134.11	1.5382	0.9984
	100 mg $BaTiO_3$	52.084	1.2028	0.99839

Tafel polarisation analysis was performed to further evaluate the influence of $BaTiO_3$ nanoparticle loading on the corrosion behaviour of MS in 2 M HCl. The results, summarised in Table 5, reveal clear trends in corrosion potential (E_{corr}), corrosion current density (i_{corr}), polarisation resistance (Rp), and inhibition efficiency (η%). For the bare MS plate, the E_{corr} value of –1.247 V and a high i_{corr} of 0.00181 A correspond to a low polarisation resistance (12.86 Ω) and a corrosion rate of 22.49 mm/year, confirming severe corrosion activity in the acidic medium. Upon coating with 25 mg $BaTiO_3$, a substantial shift of E_{corr} towards the positive direction (–0.359 V) was observed, along with a decrease in i_{corr} to 0.00106 A. This resulted in an increased polarisation resistance (21.18 Ω) and a corrosion inhibition efficiency of 41.35 %, reflecting improved protective coverage that reduced anodic dissolution.

The most pronounced improvement occurred at a 50 mg $BaTiO_3$ loading, where E_{corr} shifted further to –0.298 V, R_p increased markedly to 38.09 Ω, and η% reached 85.14 %. This indicates that at this intermediate loading, the coating achieves optimal compactness and uniformity, thereby minimising defect pathways and effectively blocking chloride ion penetration [38–40].

Table 5. Polarisation and electrochemical behaviour of the MS plate with various $BaTiO_3$ NPs loading.

Medium	Substrate	Ecorr (V)	Icorr (A)	Polarisation Resistance (Ω)	Corrosion rate (mm/year)	Efficiency (%)
2 M HCl	Bare	–1.247	0.00181	12.86	22.49	-
	25 mg $BaTiO_3$	–0.359	0.00106	21.18	13.19	41.35
	50 mg $BaTiO_3$	–0.298	0.00163	38.09	3.34	85.14
	75 mg $BaTiO_3$	–0.459	0.00169	8.97	20.09	7.06
	100 mg $BaTiO_3$	–0.577	0.02958	3.81	21.44	4.6

In contrast, higher loadings of 75 mg and 100 mg $BaTiO_3$ resulted in performance deterioration. For 75 mg, E_{corr} shifted back towards the negative side (–0.459 V), R_p decreased to 8.97 Ω, and η% dropped sharply to 7.06%. This reduction in protective performance can be attributed to excessive particle accumulation leading to coating heterogeneity, microcrack formation, and weakened adhesion. The 100 mg loading exhibited the poorest performance among the coated samples, with a significantly negative Ecorr of –0.577 V, a very high icorr (0.02958 A), a low Rp (3.81 Ω), and minimal inhibition efficiency (4.6%), likely due to extensive coating defects that accelerate localised corrosion.

4. Conclusions

In the present study, $BaTiO_3$ nanoparticles prepared via hydrothermal synthesis were effectively applied as protective coatings to enhance the corrosion resistance of metallic substrates, with emphasis on mild steel (MS) plates. The study revealed that while $BaTiO_3$ coatings significantly enhanced corrosion resistance in neutral and alkaline media, their performance in acidic environments required further improvement. To address this, an optimisation strategy was employed by systematically varying $BaTiO_3$ loading on MS plates, identifying an intermediate concentration as the most effective for achieving dense, defect-minimised coatings with strong adhesion and enhanced barrier properties. This optimised formulation provided the best balance between coating compactness and structural integrity, thereby maximising protection against chloride and proton attack. Moving forward, research will explore hybrid coatings by combining $BaTiO_3$ with complementary nanomaterials, surface

functionalisation to improve nanoparticle dispersion, and long-term durability assessments under cyclic environmental conditions to validate industrial applicability. Such efforts are expected to advance $BaTiO_3$-based systems as sustainable, high-performance solutions for corrosion protection in demanding service environments.

Acknowledgmen

The authors also acknowledge the DST-FIST (SR/FST/College-235/2014) and (SR/FST/College/2023/1423) for providing financial assistance to develop the research facilities at the Department of Nanoscience and Technology, K.S. Rangasamy College of Technology.

Funding

This research received no external funding.

Conflict of Interes

The authors declare no conflict of interest.

References

[1] O. S. I. Fayomi, I. G. Akande, S. Odigie, Journal of Physics: Conference Series **1378**(2), 022037(2019). https://doi.org/10.1088/1742-6596/1378/2/022037
[2] O. O. Joseph, S. Banjo, S. A. Afolalu, K. O. Babaremu, AIP Conference Proceedings **2452**(1), 020001(2022). https://doi.org/10.1063/12.0000000
[3] G. E. C. Bell, M. Akhoondan, S. Pool, A. Smith, Pipelines **2017**, 389(2017). https://doi.org/10.1061/9780784480892.039
[4] B. Vaghefinazari, E. Wierzbicka, P. Visser, R. Posner, R. Arrabal, E. Matykina, M. Mohedano, C. Blawert, M. L. Zheludkevich, S. V. Lamaka, Materials **15**(23), 8489(2022). https://doi.org/10.3390/ma15238489
[5] P. V. P, M. Al-Maadeed, Materials **12**(17), 2754(2019). https://doi.org/10.3390/ma12172754
[6] S.-I. Pyun, ChemTexts **7**(2), 8(2021). https://doi.org/10.1007/s40828-020-00121-y
[7] A. A. Farag, Corrosion Reviews **38**(1), 67(2020). https://doi.org/10.1515/corrrev-2019-0011
[8] D. Vasudevan, A. Kumaravel, A. Murugesan, A. Mugil, B. Karthi, K. K. Kumar, Exfoliated carbon nitrides for corrosion prevention in radiators: temperature-dependent corrosion analysis, 18(3), https://doi.org/10.15251/DJNB.2023.183.985
[9] M. A. A. Khan, O. M. Irfan, F. Djavanroodi, M. Asad, Sustainability **14**(15), 9502(2022). https://doi.org/10.3390/su14159502
[10] T. Miri, D. Seifzadeh, Z. Rajabalizadeh, Surface and Coatings Technology **477**, 130241(2024). https://doi.org/10.1016/j.surfcoat.2023.130241
[11]D. Vasudevan , D. Senthil Kumar, M. Venkatesan, A. Kumaravel, P. Dineshkumar, A. Sankar, Study of reduced graphene oxide-based nanofluids properties for heat transfer applications, 20(2), https://doi.org/10.15251/DJNB.2025.202.633.
[12] B. Lin, J. Wang, H. Zhang, Y. Wang, H. Zhang, J. Tang, J. Hou, H. Zhang, M. Sun, Corrosion Science **197**, 110084(2022). https://doi.org/10.1016/j.corsci.2022.110084
[13] K. Kandasamy, S. Surendhiran, K. S. G. Jagan, G. S. Kumar, Y. A. S. Khadar, P. Rajasingh, Applied Surface Science Advances **13**, 100364(2023). https://doi.org/10.1016/j.apsadv.2022.100364
[14] K. S. G. Jagan, S. Surendhiran, S. Savitha, T. M. Naren Vidaarth, A. Karthik, N. Lenin, R. Senthilmurugan, Inorganic Chemistry Communications **175**, 114206(2025). https://doi.org/10.1016/j.inoche.2025.114206
[15] F. Marashi-Najafi, J. Khalil-Allafi, S. Mahdavi, Journal of Materials Research and Technology **26**, 6823(2023). https://doi.org/10.1016/j.jmrt.2023.09.071
[16] M. Naveena, S. J. Muthiya, P. Divya, P. Sudhakar, Mahesh, Manjunath, Ionics **31**(2), 611(2025). https://doi.org/10.1007/s11581-024-05907-5
[17] Anonymous, Rafidain Journal of Engineering Sciences **2**(1), 32(2024). https://doi.org/10.61268/d2a1h438
[18] M. H. Muhamad Zulkflee, H. Mamat, Journal of the Indian Chemical Society **101**(5), 101462(2024). https://doi.org/10.1016/j.jics.2024.101462
[19] F. Marashi-Najafi, J. Khalil-Allafi, S. Mahdavi, M. R. Etminanfar, V. Khalili, A. B. Parsa, Progress in Organic Coatings **186**, 107978(2024). https://doi.org/10.1016/j.porgcoat.2023.107978

[20] D. Mewada, Materials Today: Proceedings **54**, 923(2022). https://doi.org/10.1016/j.matpr.2021.11.252
[21] M. M. Salem, M. A. Darwish, A. M. Altarawneh, Y. A. Alibwaini, R. Ghazy, O. M. Hemeda, D. Zhou, E. L. Trukhanova, A. V. Trukhanov, S. V. Trukhanov et al., RSC Advances **14**(5), 3335(2024). https://doi.org/10.1039/d3ra05885a
[22] S. Mustapha, M. M. Ndamitso, A. S. Abdulkareem, J. O. Tijani, D. T. Shuaib, A. K. Mohammed, A. Sumaila, Advances in Natural Sciences: Nanoscience and Nanotechnology **10**(4), 045013(2019). https://doi.org/12.1088/2043-6254/ab52f7
[23] B. Suherman, F. Nurosyid, Khairuddin, D. K. Sandi, Y. Irian, Journal of Physics: Conference Series **2190**, 012006(2022). https://doi.org/10.1088/1742-6596/2190/1/012006
[24] R. Dewi, Y. Hamzah, Y. Manik, F. Ziliwu, N. I. Simbolon, H. Syajali, S. Maulidya, Y. Ningrum, H. Fatanah, Sintechcom **4**(3), 79(2024). https://doi.org/10.59190/stc.v4i3.268
[25] H. Aldulaimi, G. Pircheraghi, A. Nemati, Polymer Composites **45**(11), 9919(2024). https://doi.org/10.1002/pc.28448
[26] S. Ali, H. Ali, M. Afaq, K. Mehmood, M. Uzair, W. Ahmad, Materials Science in Semiconductor Processing **181**, 108606(2024). https://doi.org/10.1016/j.mssp.2024.108606
[27] U. Kumar, D. Padalia, P. Bhandari, P. Kumar, L. Ranakoti, T. Singh, L. Lendvai, Polymers **14**(21), 4664(2022). https://doi.org/10.3390/polym14214664
[28] D. A. Wissa, A. A. Ward, S. A. Gad, A. M. Moustafa, N. N. Rozik, A. Nassar, S. S. Ibrahim, S. A. Khairy, S. L. Abd-El-Messieh, Journal of Cluster Science 36 (2025). https://doi.org/10.1007/s10876-025-02855-6
[29] X. Pang, T. Wang, B. Liu, X. Fan, X. Liu, J. Shen, C. Zhong, W. Hu, International Journal of Minerals, Metallurgy and Materials **30**(7), 1407-1416(2023). https://doi.org/10.1007/s12613-023-2614-9
[30] A. Moradi, R. Ansari, M. K. Hassanzadeh-Aghdam, S. Sahmani, Composite Structures **370**, 119385(2025). https://doi.org/10.1016/j.compstruct.2025.119385
[31] R. Ye, Z. Wang, Y. Xue, J. Kang, T. Zhao, Journal of Materials Science: Materials in Electronics **35**, 13472(2024). https://doi.org/10.1007/s10854-024-13472-w
[32] M. Nawaz, S. Ahmad, M. G. Taryba, M. F. Montemor, R. Kahraman, R. A. Shakoor, Progress in Organic Coatings **195**, 108659(2024). https://doi.org/10.1016/j.porgcoat.2024.108659
[33] A. O. Alao, A. P. Popoola, O. Sanni, Journal of Bio- and Tribo-Corrosion **8**(4), 99(2022). https://doi.org/10.1007/s40735-022-00665-1
[34] Z. Liu, B. Zhang, H. Yu, Z. Zhang, W. Jiang, Z. Ma, Coatings **12**(11), 1749(2022). https://doi.org/10.3390/coatings12111749
[35] T. V. Nguyen, V. Do Truc, T. A. Nguyen, D. L. Tran, Anti-Corrosion Methods and Materials **71**(3), 225(2024). https://doi.org/10.1108/acmm-06-2023-2835
[36] E. Seyran, G. Tüzün, S. Çetinkaya, B. Tüzün, in Innovations in Nanomaterials-Based Corrosion Inhibitors, IGI Global, 238(2024). https://doi.org/10.4018/979-8-3693-3088-3.ch012
[37] S. Ahmad, M. Nawaz, S. Mohammad, R. A. Shakoor, R. Kahraman, T. M. Al Tahtamouni, Surface and Coatings Technology **476**, 130172(2024). https://doi.org/10.1016/j.surfcoat.2023.130172
[38] N. Raghavendra, Journal of Bio- and Tribo-Corrosion **10**(4), 71(2024). https://doi.org/10.1007/s40735-024-00889-3
[39] B. U. Oreko, S. O. Okuma, NIPES Journal of Science and Technology Research **7**(3), 245(2025). https://doi.org/10.37933/nipes/7.3.2025.1449
[40] T. V. Nguyen, D. L. Tran, T. A. Nguyen, T. T. H. Nguyen, P. H. Dao, V. P. Mac, M. T. Do, T. M. Nguyen, T. M. L. Dang, Anti-Corrosion Methods and Materials **69**(5), 514(2022). https://doi.org/10.1108/acmm-03-2022-2629